RESEARCH ARTICLE

CHEMISTRY

Graphdiyne-based metal atomic catalysts for synthesizing ammonia

Huidi Yu[1], Yurui Xue[1,2,*], Lan Hui[1], Chao Zhang[1], Yan Fang[1], Yuxin Liu[1], Xi Chen[1], Danyan Zhang[1], Bolong Huang[3,*] and Yuliang Li[1,4,*]

ABSTRACT

Development of novel catalysts for nitrogen reduction at ambient pressures and temperatures with ultrahigh ammonia (NH_3) yield and selectivity is challenging. In this work, an atomic catalyst with separated Pd atoms on graphdiyne (Pd-GDY) was synthesized, which shows fascinating electrocatalytic properties for nitrogen reduction. The catalyst has the highest average NH_3 yield of $4.45 \pm 0.30 \, \mathrm{mg_{NH_3} \, mg_{Pd}^{-1} \, h^{-1}}$, almost tens of orders larger than for previously reported catalysts, and 100% reaction selectivity in neutral media. Pd-GDY exhibits almost no decreases in NH_3 yield and Faradaic efficiency. Density functional theory calculations show that the reaction pathway prefers to perform at the (Pd, C1, C2) active area because of the strongly coupled (Pd, C1, C2), which elevates the selectivity via enhanced electron transfer. By adjusting the *p–d* coupling accurately, reduction of self-activated nitrogen is promoted by anchoring atom selection, and side effects are minimized.

Keywords: graphdiyne, atomic catalyst, two-dimensional carbon material, ammonia, nitrogen reduction reaction

[1]Institute of Chemistry, Chinese Academy of Sciences, Beijing 100190, China; [2]Science Center for Material Creation and Energy Conversion, School of Chemistry and Chemical Engineering, Institute of Frontier and Interdisciplinary Science, Shandong University, Jinan 250100, China; [3]Department of Applied Biology and Chemical Technology, The Hong Kong Polytechnic University, Hong Kong, China and [4]University of Chinese Academy of Sciences, Beijing 100049, China

*Corresponding authors. E-mails: xueyurui@iccas.ac.cn; ylli@iccas.ac.cn; bhuang@polyu.edu.hk

INTRODUCTION

Ammonia (NH_3), an indispensable raw material in industrial production, has always occupied an important position in basic chemical industry, and is also an important source of chemical fertilizer in agricultural production [1–3]. Unfortunately, traditional production of NH_3 must operate at high pressures and temperatures, which is very energy-consuming. Electrochemical catalytic nitrogen reduction reaction (ECNRR) in aqueous electrolytes at ambient conditions provides an ideal method for clean and efficient conversion of N_2 to energy-rich NH_3 [4–7]. However, there are some key scientific and technical issues with this approach, and the NH_3 yield (Y_{NH_3}) and Faradaic efficiency (FE) are still very low. To solve these major issues and promote efficient conversion of N_2 to NH_3, efficient catalysts that can drive ECNRR at low overpotential with high selectivity, Y_{NH_3}, FE and stability are in great demand.

Electrocatalysts comprising singly-dispersed metal atoms and supporting materials have shown high catalytic activity and selectivity in various reactions, because of their atomically distributed active sites [8–21]. Although the rapid development of single-atom catalysts has introduced many new opportunities in terms of new catalytic science, knowledge and concepts, there remain some important scientific issues to be solved, such as the precise structure of the support materials, the valence of the supported metal atoms and the structure, the high dispersion distribution of the metal single atoms and so on.

Very recently, Li and coworkers reported the first zero-valent atomic catalysts (AC) [20,21]. An important finding that has drawn great attention is that zero-valent metal atoms can be anchored on graphdiyne surfaces [22–31]. The AC exhibits high stability and catalytic activity and represents the emergence of a new generation of catalysts, and there is a drive to understand the mechanism, reaction process and properties of atomic catalysis. In this study, we demonstrate that highly selective and active NH_3 production can be achieved using a zero-valence atom catalyst based on graphdiyne, Pd-GDY, to activate the N_2 and react with water at

room temperature and pressure. Experimental and theoretical results solidly confirm the unique chemical and electronic structures and zero-valence state of this electrocatalyst. The strong orbital interactions between Pd atoms and neighboring C sites lead to a strong electronegative reduction character for ECNRR. The downshifted s-band from the electronic structure arises from the elimination of non-bonding lone-pair N2-2s orbitals through N-hydrogenation to suppress HER electronically. The designed Pd-GDY AC presents significantly improved ECNRR performance compared with previously reported catalysts. This study could provide a promising strategy for designing and synthesizing highly efficient electrocatalysts for producing NH_3 at room temperature and ambient pressures.

RESULTS AND DISCUSSION

Pd-GDY was synthesized through a self-reduction strategy. Figure 1 shows the synthesis and reusability schematic of Pd-GDY for the electrochemical nitrogen reduction reaction. As can be seen from the scanning electron microscopy (SEM) images (Supplementary Fig. S1), graphdiyne fibers with porous surface interweave in a three-dimensional manner forming three-dimensional flexible electrodes.

No Pd particles or clusters can be observed in the SEM (Fig. 2a and Supplementary Fig. S2), high-resolution transmission electron microscopy (HRTEM) (Fig. 2b and Supplementary Fig. S3),

scanning transmission electron microscopy (STEM, Fig. 2c) and high-angle annular dark-field (HAADF) STEM (Fig. 2d–g and Supplementary Fig. S4) images. Energy-dispersive X-ray spectroscopy mapping results (Fig. 2c) reveal the uniform distribution of Pd and C atoms in the sample. In the HAADF images, the bright dots gave an average size of 0.36 ± 0.01 nm (Supplementary Fig. S5), confirming that each dot is an individual Pd atom. The possible anchoring sites of Pd atoms on GDY are shown in Supplementary Fig. S6, as revealed by our detailed computational calculations in which all possible placements of the Pd on GDY were fully examined. The optimal anchoring site is determined based on comparison of formation energies between different anchoring sites, in that the lowest formation energy of the anchoring site of -0.99 eV as the presented position will be the optimal placement for Pd on GDY. Inductively coupled plasma optical emission spectroscopy (ICP-OES) measurements showed an average mass loading of 1.02 ± 0.04 wt.%. Figure 2h and i shows the X-ray absorption near-edge structure (XANES) profiles for Pd-GDY along with corresponding reference samples (Pd foil and PdO). For the Pd K-edge spectrum, the absorption threshold position of Pd-GDY is located at the same position as Pd metal but a more negative position than PdO (Fig. 2h). In addition, the first derivative XANES for Pd-GDY is similar to that of metallic Pd (Fig. 2i). These results strongly indicate that the valence states for the Pd atoms in Pd-GDY metals are zero. The extended X-ray absorption fine structure (EXAFS) spectrometry results (Supplementary Fig. S7) showed that there was only one peak at around 1.5 to 2 Å arising from the Pd~C contribution, and that no peak contributing to the Pd–Pd (around 2~3 Å) could be observed. These demonstrate that the Pd atoms are individually anchored on GDY and exhibit zero-valence state (Supplementary Fig. S8).

We used X-ray photoelectron spectroscopy (XPS) and Raman spectra to characterize the chemical composition and quality of as-synthesized samples. The XPS survey spectra show the only existence of carbon (Supplementary Fig. S9), except for oxygen signal from the adsorption of air. The C 1s XPS spectrum of Pd-GDY can be divided into sp^2-C (284.5 eV), sp-C (285.1 eV), C=O (288.3 eV), COO (286.7 eV) and π–π transition (291.2 eV) peaks (Supplementary Fig. S10a). Compared with pure GDY (Supplementary Fig. S10b), a newly formed peak at 291.2 eV was observed, which can be attributed to the electronic transitions induced by the anchoring of Pd atoms. The ratio of intensity of sp^2/sp-carbon is 0.5, revealing the integrity of the GDY structure in Pd-GDY. As shown in
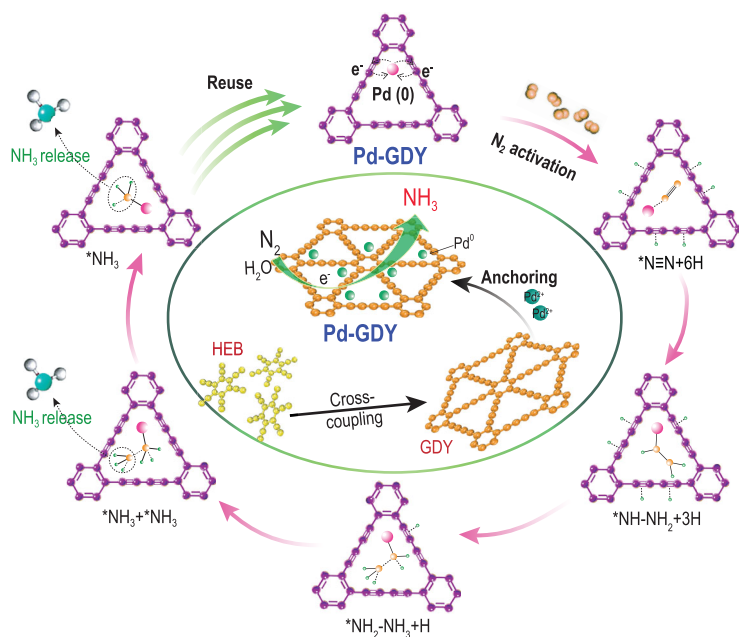
Figure 1. Schematic of the synthesis (central green circle) and reusability of the Pd-GDY electrocatalyst for the ammonia production.
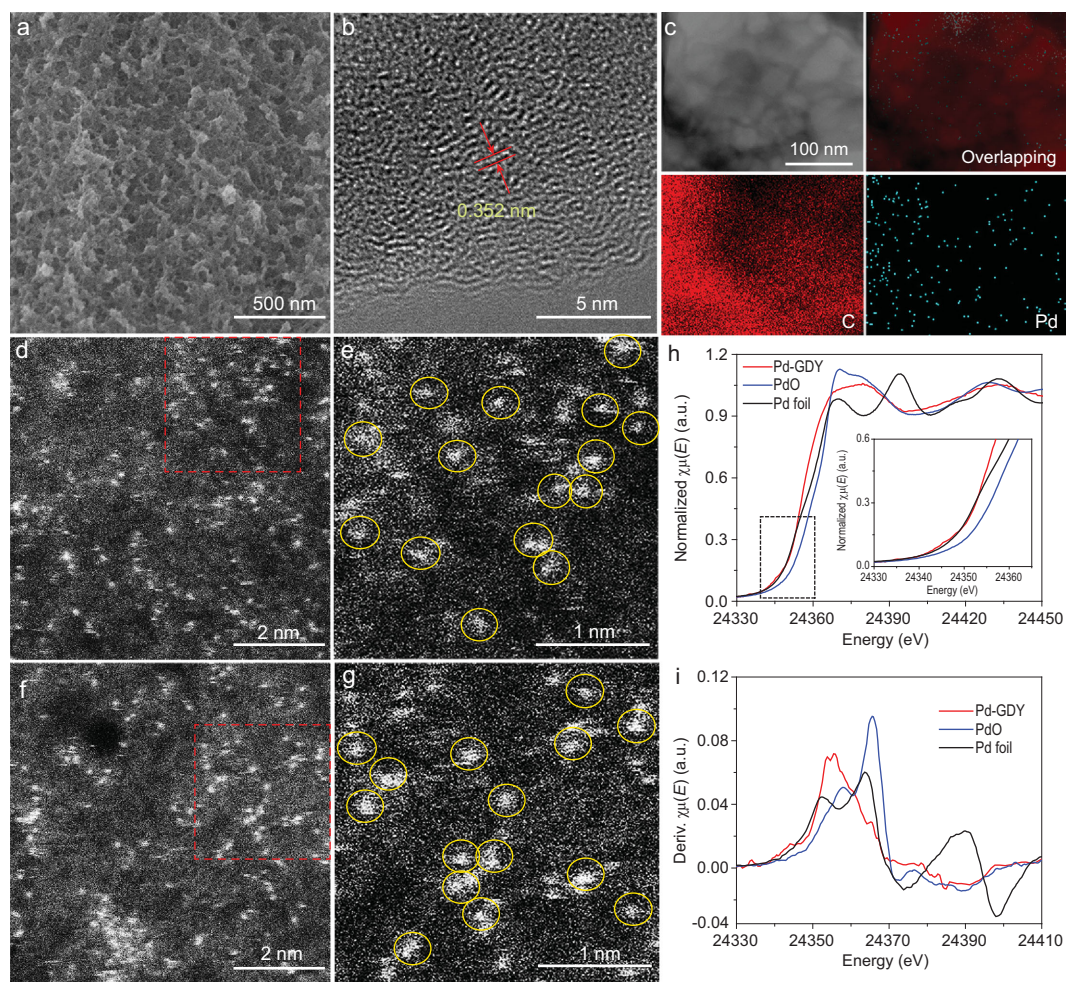
Figure 2. (a) SEM, (b) HRTEM, (c) elemental mapping, and (d and f) HADDF-STEM images of Pd-GDY. (e and g) Enlarged images of the red square areas in images (d) and (f), respectively. (h) The experimental K-edge XANES spectra (inset: magnified image) and (i) the first derivative curves of Pd-GDY, Pd foil and PdO.

Supplementary Fig. S11, the Pd-GDY shows a lower valence band (VB) with a smaller energy at 1.73 eV than that of pure GDY (2.26 eV), indicating the enhanced conductivity of Pd-GDY. Raman spectra provide information on the structural changes of carbon materials. The intensity of the D and G bands of GDY and Pd-GDY changed (Supplementary Fig. S12). The D band to G band intensity ratio increased from 0.73 (GDY) to 0.82 (Pd-GDY), which suggests the presence of more defective sites in Pd-GDY, indicating the formation of more active sites, which have been demonstrated to be helpful for improving catalytic activity [32,33].

Based on the above inspiring findings, the EC-NRR experiments were carried out in 0.1 M Na$_2$SO$_4$ (pH = 7) aqueous solution at room temperature and atmospheric pressure using an H-type electrolytic cell separated by the Nafion 117 membrane (Supplementary Fig. S13). The catalyst loading of Pd-GDY is 2.7 μg$_{metal}$ cm^{-2}, and the geometric

area is 2.0 cm^2. The NH$_3$ was determined using an indophenol blue method [34] and calibration curves with reliable sensitivity and good linear relationship were obtained (Supplementary Fig. S14). The ECNRR of Pd-GDY starts at around 0.2 V versus RHE in N$_2$-saturated 0.1 M Na$_2$SO$_4$ solution (Supplementary Fig. S15). Only NH$_3$ (no by-product of N$_2$H$_4$) can be detected in this work (Supplementary Figs S16 and S17), revealing the ultra-high selectivity of Pd-GDY in the ECNRR process. The NH$_3$ yielding rate (Y$_{NH3}$) and the Faradaic efficiency (FE) rise with increasing cathodic potential until -0.16 V versus RHE (Fig. 3a and b), at which the highest Y$_{NH3}$ of 4.45 $\pm$ 0.30 mg$_{NH3}$ mg$_{Pd}^{-1}$ h^{-1} (1.97 $\pm$ 0.13 $\times$ 10^{-10} mol cm^{-2} s^{-1}, normalized by geometric surface area) and FE up to 31.62 $\pm$ 1.06% were achieved (Supplementary Table S1). These values are larger than for all previously reported ECNRR catalysts working under ambient conditions including Au/TiO$_2$
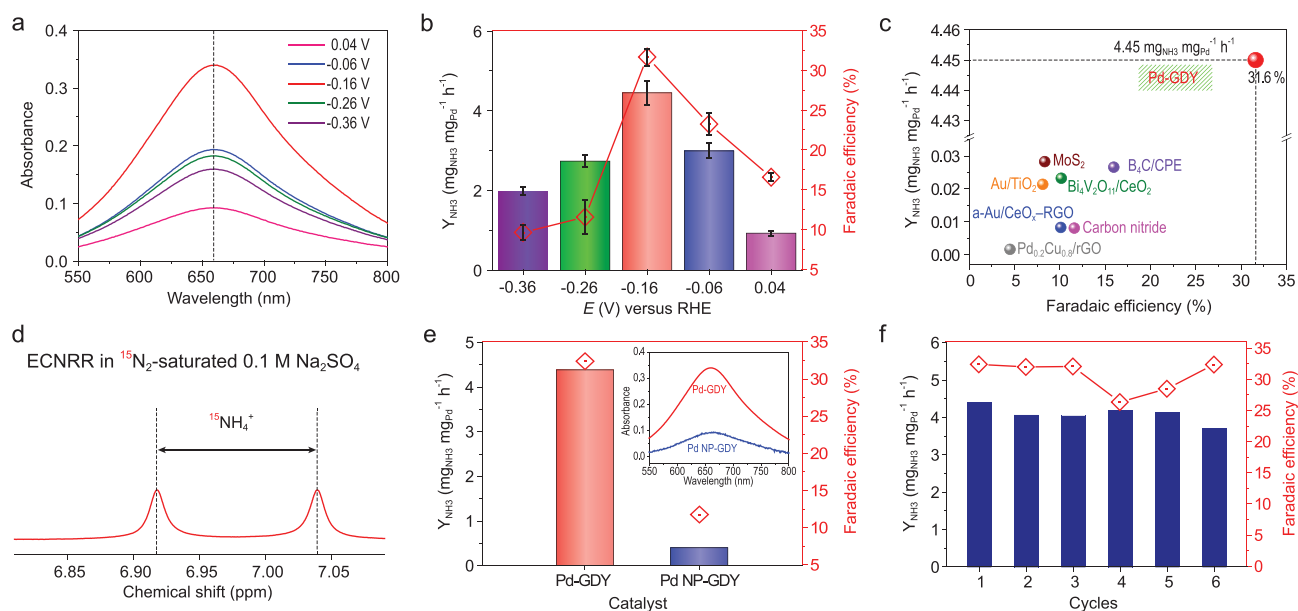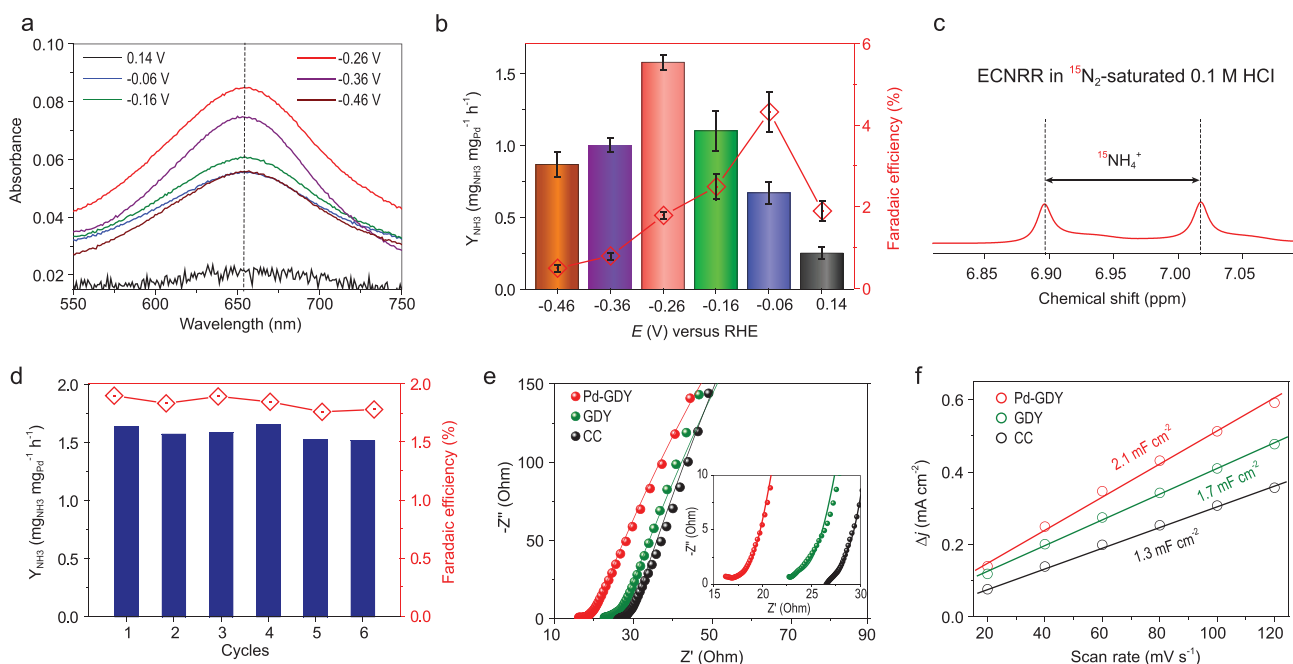
Figure 3. (a) UV–Vis absorption spectra of the 0.1 M Na_2SO_4 electrolytes after ECNRR at different potentials for 2 h. (b) Y_{NH3} and FEs at applied potentials in 0.1 M Na_2SO_4. Error bars represent calculated standard deviation from independent experiments (at least three times). (c) Comparison of the ECNRR performance of Pd-GDY with others. Error bars represent calculated standard deviation from independent experiments (at least three times). (d) ^1H-^{15}N NMR spectra of 0.1 M Na_2SO_4 after ECNRR under $^{15}N_2$ with Pd-GDY as catalyst. (e) Y_{NH3}, FEs and corresponding UV–Vis absorption spectra (inset) of Pd-GDY and Pd NP/GDY catalysts after 2 h electrolysis at −0.16 V versus RHE. (f) Stability test of Pd-GDY at −0.16 V versus RHE in 0.1 M Na_2SO_4 under ambient conditions.

($Y_{NH3} = 21.4\ \mu g_{NH3}\ mg_{cat.}^{-1}\ h^{-1}$, FE = 8.11%) [6], THH Au NRs ($Y_{NH3} = 2.69 \times 10^{-11}\ mol\ cm^{-2}\ s^{-1}$, FE = 4.02%) [35], $Bi_4V_2O_{11}/CeO_2$ ($Y_{NH3} = 23.21\ \mu g_{NH3}\ mg_{cat.}^{-1}\ h^{-1}$, FE = 10.16%) [36], Ru SAs/N-C ($Y_{NH3} = 120\ \mu g_{NH3}\ mg_{cat.}^{-1}\ h^{-1}$, FE = 29.6%) [37] and Ru NC ($Y_{NH3} = 3.6\ mg_{NH3}\ mg_{cat.}^{-1}\ h^{-1}$, FE = 21%) [38], and Pd-based EC-NRR catalysts such as Pd/C ($Y_{NH3} = 4.9\ \mu g_{NH3}\ mg_{cat.}^{-1}\ h^{-1}$, FE = 8.2%) [39], $Pd_{0.2}Cu_{0.8}/rGO$ ($Y_{NH3} = 2.8\ \mu g_{NH3}\ mg_{cat.}^{-1}\ h^{-1}$, FE = 4.5%) [40], Pd_3Cu_1 alloy ($Y_{NH3} = 39.9\ \mu g_{NH3}\ mg_{cat.}^{-1}\ h^{-1}$, FE = 1.22%) [41], and even compared favorably with those working at higher temperatures/pressures (Fig. 3c; Supplementary Tables S2 and S3) [42]. With further increase of the negative potentials, the Y_{NH3} and FE decreased sharply, which can be attributed to competition between EC-NRR and HER [21,43]. Control experiments were performed to determine the origin of the detected NH_3. The pristine GDY yielded limited NH_3 (Y_{NH3}: $5.44 \times 10^{-12}\ mol\ cm^{-2}\ s^{-1}$; FE: 1.65%; Supplementary Fig. S17a,b) and CC substrate yielded almost no NH_3 (Supplementary Fig. S17a). No NH_3 can be detected in Ar-saturated electrolyte (Supplementary Fig. S17c) and at the open-circuit potential (Supplementary Fig. S17d). ^{15}N-labelling experiments were performed using $^{15}N_2$ as the feeding gas to confirm the ammonium formed from the reduction of N_2. Only $^{15}NH_4^+$ (doublet peak) was

observed from the ^1H nuclear magnetic resonance (^1H-NMR) results (Fig. 3d). These results revealed that all detected NH_3 comes from reduction of N_2 molecules by the Pd-GDY catalyst. The fact that the Y_{NH3} and FE of Pd-GDY are almost 10 and 3 times larger than those of palladium nanoparticle-modified GDY (Pd NP/GDY, Supplementary Fig. S18) demonstrates the superiority of isolated zero-valence Pd atoms over bulk Pd nanoparticles toward efficiently catalyzing ECNRR (Fig. 3e). In addition to excellent catalytic activity and selectivity, long-term stability is another essential criterion for an electrocatalyst in practical applications. It was observed that the NH_3 yield rate and FE of Pd-GDY exhibited no obvious change after six successive catalytic cycles (Fig. 3f, Supplementary Fig. S19), and the total NH_3 yield increased linearly with reaction time (Supplementary Fig. S20). Comprehensive characterizations (Supplementary Fig. S21) on the sample obtained after stability test showed good preservation of the morphology and structure, revealing its robust nature.

Electrolytes are considered to have significant effects on the ECNRR selectivity and activity [39,43–45]. Neutral and basic electrolytes with limited proton transfer rate can effectively improve the ECNRR selectivity. However, in acidic electrolytes, the ECNRR selectivity could be kinetically limited because of the high availability of protons;

Figure 4. (a) UV–Vis absorption spectra of the 0.1 M HCl electrolytes after ECNRR at different potentials for 2 h. (b) Y_{NH3} and FEs at applied potentials in 0.1 M HCl. (c) ^1H-^{15}N NMR spectra of 0.1 M HCl after ECNRR under $^{15}N_2$ with Pd-GDY as catalyst. (d) Stability test of Pd-GDY at -0.26 V versus RHE under ambient conditions. (e) Measured and fitted impedance data of the samples. (f) Plot of current density versus scan rates of 20, 40, 60, 80, 100 and 120 mV s^{-1}, respectively.

the rate of the HER increases significantly with the increase of applied potentials, in which most protons or H_2O are converted to H_2 rather than NH_3, resulting in great decreases in reaction selectivity. Efforts have recently been devoted to improving ECNRR performance in acidic electrolytes [37,44,46–48]. However, the Y_{NH3} and Faradaic efficiencies of reported ECNRR electrocatalysts are still very low (Supplementary Tables S2 and S3). Because of these limitations, it is of significant importance to develop an electrocatalyst with high selectivity and activity in acidic electrolytes for efficient ECNRR.

We then studied the ECNRR activity of Pd-GDY in 0.1 M HCl solution (Fig. 4a, Supplementary Fig. S22). NH_3 and N_2H_4 were determined using a spectrophotometry method, and the calibration curves are shown in Supplementary Fig. S23. Pd-GDY also shows high selectivity toward formation of NH_3 (without N_2H_4 formation) in acidic media (Supplementary Figs S22b and S24). As shown in Fig. 4b, the average NH_3 yield rate reaches a maximum value of 1.58 ± 0.05 mg$_{NH3}$ mg$_{Pd}^{-1}$ h^{-1} [$(6.99 \pm 0.22) \times 10^{-11}$ mol cm^{-2} s^{-1} at -0.26 V versus RHE], while it achieves the highest FE of $4.32 \pm 0.49\%$ at a cathodic potential of -0.06 V versus RHE (Supplementary Table S1). The ^{15}N isotope labelling experiments confirmed that the NH_3 was formed from reduction of N_2 (Fig. 4c), which indicates that the Pd-GDY is highly selective and active

toward ECNRR in acidic media. The FE value keeps decreasing as the applied potentials become more negative, which can be attributed to competition from the HER in acidic media. The rapid increase of current densities in polarization curves recorded in both N_2- and Ar-saturated 0.1 M HCl (Supplementary Fig. S25) also gives supportive evidence for this major interference. Despite all this, the ECNRR activity of Pd-GDY in acidic conditions still compared favorably with those of most previously reported catalysts (Supplementary Tables S2 and S3) such as MoS_2 ($Y_{NH3} = 8.48^{-11}$ mol cm^{-2} s^{-1}, FE $= 0.096\%$). In addition, both Y_{NH3} and FE of Pd-GDY show negligible degradation after six consecutive tests, confirming reliable stability of Pd-GDY in acidic media (Fig. 4d). Electrochemical impedance spectroscopy (EIS) was conducted to offer more insight into the catalytic behaviors. The impedance data were recorded and analyzed using a R(QR)(QR) equivalent circuit model (Supplementary Table S4). From Fig. 4e, Pd-GDY shows the lowest solution resistance (R_s, 10.41 Ω) and charge transfer resistance (R_{ct}, 3501 Ω) over GDY (R_s, 15.70 Ω; Rct, 4658 Ω) and CC (R_s, 26.5 Ω; Rct, 8933 Ω), indicating a more kinetically favorable ECNRR for Pd-GDY than others. Electrochemically active surface area (ECSA) was further estimated by determining the electrochemical double-layer capacitance (C_{dl}) through a cyclic voltammetry method
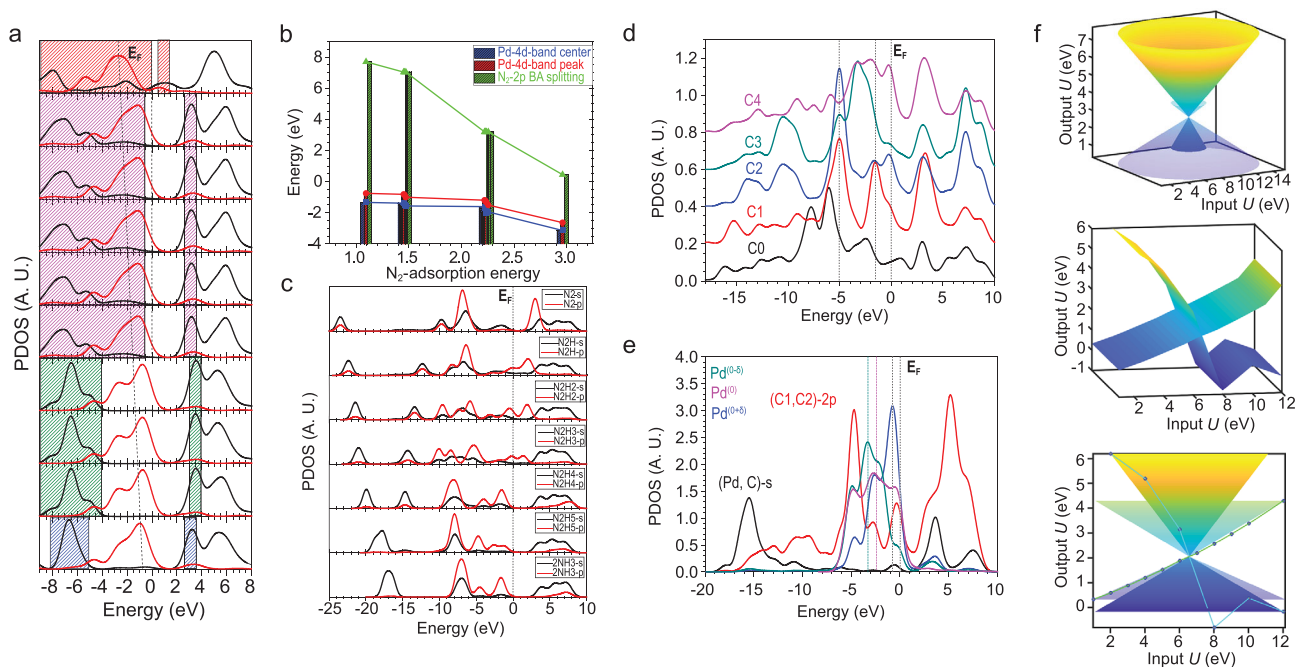
Figure 5. (a) PDOSs evolutions of site-dependent energetic preference N-fixation on the GDY-Pd system. The energetic preference sequence follows the sequence of blue (strongly favorable), green, pink and red (unfavorable) shaded area. (b) The variation behavior of the Pd-4d band center, Pd-4d band peak position and N_2–2p BA splitting related to the N_2-adsorption energy. (c) PDOSs of s- and p- bands of all related N-species and adsorbing H among the ECNRR steps. (d) PDOSs of p-orbitals of C0, and C1–C4. The C0 is the C site of benzene ring and C1–C4 are labelled sequentially following the C0 along the C-chain bonding with Pd. (e) PDOSs of s, p and d orbitals from Pd-(C1, C2) bonding motifs from GDY-Pd with consideration of different charge populations. (f) The orbital potential energy projections (U_{out1} and U_{out2}) for Pd-4d within a singly anchoring site under the planar and round constant electrode potential distribution.

(Supplementary Fig. S26). The C_{dl} value of Pd-GDY is 2.1 mF cm^{-2} (Fig. 4f), which is larger than those of pure GDY (1.7 mF cm^{-2}) and CC (1.3 mF cm^{-2}), implying an increase of the active site number in the Pd-GDY catalyst.

The origin of the outstanding catalytic activities of the samples was further studied with computational calculations (see Methods for details). The bonding and anti-bonding orbitals near the Fermi level (E_F) are demonstrated for the cases of Pd-GDY, HER and ECNRR. We found that the (Pd, C1, C2) sites are electron-rich regions, exhibiting the localized p–d coupled electronic orbital. The variation of the real-spatial distribution of charge density distribution indicates site-to-site charge migration and redistribution between the Pd-GDY and N/H-species (Fig. 5a). The interplay of Pd-4d and N_2–2p orbitals was illustrated with the projected partial density of states (PDOSs). We found that the preference of N_2-adsorption on the Pd-GDY interacting with Pd-4d orbitals indeed follows the farthest p–d separation rather than p–d orbital overlapping. This is evidently different from the adsorption preference of O-species. Such an anomalous trend implies that the on-site effective screening Coulomb repulsion potential is a determining factor

existing between Pd-4d^{10} and N_2-$(2s^2, 2p^3)$. This arises because the non-bonding lone-pair N_2–2s-orbitals are highly active, participating within the ECNRR process for hydrogenation bonding. The fulfilled Pd-4d^{10} is an electron-rich center for evident site-to-site charge migrations, exhibiting substantially strong electronegative activity (ENA). Such strong ENA induces high chemical potential contrast for favorite directional electron transfer, which favors electron transfer from Pd onto N-species for N-hydrogenation rather than HER. We further interpret the underlying electronic mechanism to redirect the HER-suppression trend. The p–d coupled effective negative correlation energy matters to the subtle interplay between on-site Coulomb repulsion and ENA, which overcomes on-site Coulomb repulsion and is energetically favorable to accumulate ENA (Fig. 5a). The Pd-4d band center, Pd-4d band dominant peak, and splitting gap between bonding and anti-bonding (BA) of N_2–2p-band all exhibit the same trend to monotonically decrease with N_2-adsorption energy increases. The deep localized Pd-4d^{10}-t_{2g} component strongly couples with the N_2–2p band, resulting in a narrowing of the N_2–2p band BA splitting gap (Fig. 5b). We further demonstrate the s- and
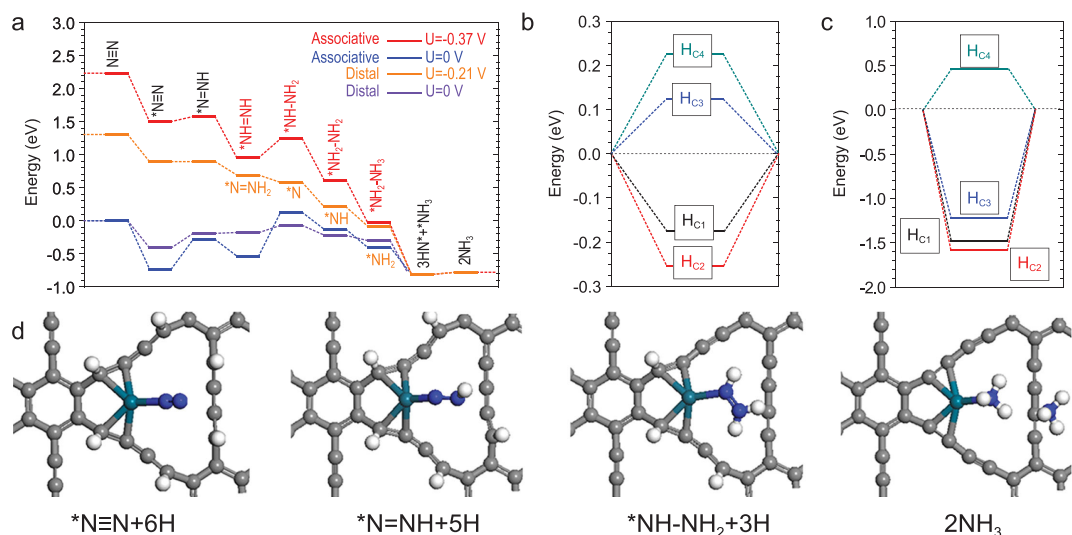
Figure 6. (a) ECNRR energetic pathway on the GDY-Pd. (b) Formation energies of H-adsorption on C sites of GDY-Pd. (c) H-chemisorption energies on C sites of GDY-Pd. (d) Structural configuration evolution of ECNRR catalysis process.

p- band variations among the N-hydrogenation process. The downshifted s-band arises from the elimination of non-bonding lone-pair N_2-2s orbitals through N-hydrogenation. The N-hydrogenation performs 0.8 eV more than the H-adsorption at the C site. Therefore, the original HER performance has been electronically suppressed (Fig. 5c). Considering the contribution of individual C sites within Pd-GDY, both C1 and C2 sites clearly show a strong 2p electronic state at E_V-5.0 eV as relay-center-like level promoting electron transfer between Pd and (C1, C2). The evident bonding and anti-bonding splitting feature at the C1 site confirms that the strong Pd-C1 interaction is indeed enhanced and further stabilized via charge transfer (Fig. 5d). The PDOSs of Pd-4d and (C1, C2)-2p orbitals presented a large overlap near the E_F, and the two dominant BA orbitals of (C1, C2) coupled the Pd-4d bands. The metallic fcc-Pd^0, $Pd^{0-\delta}$, and $Pd^{0+\delta}$ states $(0 < \delta < 1)$ were compared within the PDOSs. The $Pd^{0-\delta}$ shows 1 eV lower than the fcc-Pd^0, while $Pd^{0+\delta}$ stays 1.5 eV higher. This reveals that Pd-GDY preserves the Pd^0 state and possesses an even higher ENA than the fcc-Pd^0, which dominates the strong electronegative reduction character for ECNRR (Fig. 5e). We further determined the Pd-4d orbital information under the electrode potential of the planar and round constant potential distributions. Strong orbital interaction between Pd and neighboring C sites induces a close shell effect by way of crossover. The crossover orbital energy turns to be the equivalent point for repulsion and ENA energetic competition, which stays at 6.55 eV beyond the original energy found from fcc-Pd (2.51 eV).

This implies that the ENA has been promoted by the negative correlation to overcome the orbital repulsion (Fig. 5f).

We move on to the energetic preference of ECNRR. Benchmarked from different adsorption configurations, the pathway prefers to perform at the (Pd, C1, C2) active area. This is because the strongly coupled (Pd, C1, C2) elevates the selectivity via enhanced electron transfer, as discussed above. The Pd site dominated preferable pathway was then considered. The Pd-GDY possesses potential of $U = -0.37$ V for ECNRR and shows a mainly downhill energetic trend. Between these two parts, the Pd site dominates the optimal N-fixation and the C sites along the C-chain distribute the H-adsorption. For $U = -0.37$ V, the overall energy gain is -3.01 eV, where the NH_3-desorption is almost barrier-free of merely 0.03 eV for each NH_3. For $U = 0$ V, the path confronts the barrier at the asymmetrical N-hydrogenation step until the formation of $^*NH$-$NH_2 + 3(H^+ + e^-)$, which starts a downhill trend. This hydrogenation step determines the overall reaction barrier of 0.66 eV. The formation of $^*N = NH + 5(H^+ + e^-)$ also shows an uphill step, but a lower barrier of 0.45 eV. Therefore, the asymmetric H-desorption from the (C1, C2) sites controls the barrier acting as a potential determining step (PDS) for the ECNRR (Fig. 6a). We compared site-dependent H-adsorption energies. The C1 and C2 sites are confirmed as energetically favorable sites for H-adsorption. Further H-chemisorption energies summarize that both C1 and C2 contribute two optimal active sites for H-adsorption for efficient proton-electron charge exchange (Fig. 6b and c). From pathway analysis, we

found that the ECNRR prefers parallel hydrogenation (late N–N cleavage) over serial hydrogenation (early N–N cleavage). Further local structural configurations of the ECNRR process demonstrate that late N–N bond dissociation starts at the step of $NH_2--NH_3+(H^++e^-)$, which is advantageous for better HER suppression. This shows a consistent trend that the intermediate nitrogen-nitrogen bonding (i.e. N=N and N–N) variation ensures energetic compensation for H-desorption from the local active adsorption sites (Fig. 6d).

CONCLUSION

In summary, our experimental and theoretical results strongly support a zero-valence state of the palladium atom that can be anchored on graphdiyne surfaces. The anchoring site of a zero-valence metal atom was observed directly by XANES, and the position of the atomic site as judged by sight is in agreement with the theoretical calculation. The derivative X-ray absorption near-edge structure (XANES) of Pd-GDY is similar to that of metallic Pd, which confirms that the stable valence state of Pd atoms in the sample is zero. The zero-valence Pd atoms separated from graphdiyne show high ECNRR activity and selectivity with the highest N_2 reduction activity and average yield of NH_3 at 4.45 ± 0.30 mg$_{NH_3}$ mg$_{Pd}^{-1}$ h^{-1} under environmental conditions. Our work represents a new concept of catalysis, which is of great significance for a deeper understanding of the catalytic process and mechanism of zero-valence atomic catalysts, especially the discovery of highly selective atomic catalysts for conversion of nitrogen to ammonia at high efficiency.

We note the rapid development of single-atom catalysts in recent years, which has led to the rapid development of catalytic science. Prof. Tao Zhang [8,9,11], Prof. Jun Li [11,49,50] and Prof. Yadong Li [16,17,19] *et al.* have made many contributions to basic and applied research on single-atom catalysts, leading the progress in this field. Our study cleverly uses the advantages of the electronic and chemical structures of graphdiyne to successfully anchor transition metal and noble metal zero-valent atoms on graphdiyne, so we call this an 'atomic' catalyst. Loading zero-valent metal atoms has been an important challenge in the field of catalysts, especially for anchoring transition metal atoms. The success of loading zero-valent metal atoms on graphdiyne expands the synthesis methodology of single-atom catalysts and enriches the types of functional catalysts. The birth of zero-valent atomic catalysts is of great academic significance for us to clearly understand the anchoring process of single atoms on the support, the new catalytic process and mechanism, the inter-

action of metal atoms with the support, the energy, electron transfer and conversion in the system, and the relationship between the catalytic performance and the above scientific content. The emergence of zero-valent catalysts is a real insight into the strategies involved in the development of new single-atom catalysts. The following strategies are the principles of our later design and synthesis of highly efficient catalysts: (i) the design of support is an important basic strategy related to catalyst stability, selectivity and efficiency; (ii) the energy transfer and electron transport between the support and different metal atoms must be considered; (iii) systems theory must be developed for single-atom and atomic catalysts, and how to use machine learning to screen functionalized catalysts; (iv) in particular, it is necessary to develop highly conjugated supports to form donor-acceptor (D–A) systems with metal atoms, understand the mode of interaction of metal atoms and supports, and better understand the regular of structure and performance of the system; and (v) it must be considered how to control the amount of charge transfer in a single-atom system to realize the regulation of catalyst activity.

METHODS

Preparation of GDY electrode

GDY electrodes were prepared according to previous studies [20,21,23]. Typically, 50 mL of a pyridinic solution of hexaethynylbenzene (HEB, 0.4 mg mL^{-1}) was added very slowly to a three-necked flask containing several pieces of copper foil and carbon cloth (CC) at 110°C. After a 3-day reaction (110°C, protected from air and light), the CC was washed with hot acetone, DMF, KOH (4 M), HCl (6 M), KOH (4 M) and water, sequentially, followed by drying in a 40°C vacuum oven for 12 hours. The GDY electrodes were obtained.

Preparation of Pd-GDY

A piece of the freshly prepared GDY electrode was immersed into 35 mL H_2SO_4 aqueous solution containing 12 mg $PdCl_2$. During this process, the Pd atoms could spontaneously anchor to the GDY surface. After a 4-hour reaction, the samples were washed with 0.5 M H_2SO_4 and water in sequence, and then immediately used for ECNRR.

Characterizations

SEM images were obtained from an S-4800 field emission scanning electron microscope. TEM, HRTEM and EDX mapping data were collected

using a JEM-2100F electron microscope operating at 200 kV. (HAADF) STEM measurements were conducted on aberration-corrected cubed FET Titan Cubed Themis G2 300 or JEM-ARM200F (JEOL, Tokyo, Japan). XRD patterns were recorded using a D/max-2500 rotation anode X-ray diffractometer (Rigaku, Japan) with Cu Kα radiation (λ = 1.54178 Å). Raman measurements were performed on a Renishaw-2000 Raman spectrometer (473 nm excitation laser source). A Thermo Scientific ESCALab 250Xi instrument with monochromatic Al Kα X-ray radiation was used to perform the XPS measurements.

ECNRR measurements

ECNRR measurements were carried out on an electrochemical workstation (CHI 660E) with H-type electrolytic cell, which was separated by the Nafion 117 membrane into two chambers. The freshly prepared Pd-GDY (or other reference sample) was used as a working electrode. The catalyst loading of Pd-GDY catalyst is 2.7 μg_{metal} cm^{-2}, and the geometric area is 2 cm^2. The graphite rod and saturated calomel electrode were used as the counter and reference electrodes, respectively. 30 mL N$_2$-saturated electrolyte (0.1 M Na$_2$SO$_4$ or 0.1 M HCl) was added into the chambers. N$_2$ flow was continuously fed into the cathodic side with proper position. The catalytic activities of Pd-GDY normalized by geometric area and catalyst loading were compared with other recently reported catalysts. Chronoamperometry tests were performed under ambient conditions at different potentials.

SUPPLEMENTARY DATA

Supplementary data are available at *NSR* online.

AUTHOR CONTRIBUTIONS

Y.L proposed and supervised the project, conceived and designed the research, and critically revised the manuscript. H.Y. synthesized the catalysts, and carried out the experiments. Y.X. assisted the data analysis, organized and wrote the draft. L.H., C.Z., Y.F., Y.L., X.C. and D.Z. gave useful help during the synthesis and morphological characterization processes. B.H. conducted the theoretical calculations. All authors discussed the results and participated in analyzing the experimental results.

Conflict of interest statement. None declared.

REFERENCES

1. Kitano M, Inoue Y and Yamazaki Y *et al.* Ammonia synthesis using a stable electride as an electron donor and reversible hydrogen store. *Nat Chem* 2012; **4**: 934–40.
2. Liu C, Sakimoto KK and Colón BC *et al.* Ambient nitrogen reduction cycle using a hybrid inorganic–biological system. *Proc Natl Acad Sci USA* 2017; **114**: 6450–5.
3. Jennings J. *Catalytic Ammonia Synthesis: Fundamentals and Practice.* New York: Springer, 1991.
4. Wang Y, Yu Y and Jia R *et al.* Electrochemical synthesis of nitric acid from air and ammonia through waste utilization. *Natl Sci Rev* 2019; **6**: 730–8.
5. Brown KA, Harris DF and Wilker MB *et al.* Light-driven dinitrogen reduction catalyzed by a CdS: nitrogenase MoFe protein biohybrid. *Science* 2016; **352**: 448–50.
6. Shi MM, Bao D and Wulan BR *et al.* Au sub-nanoclusters on TiO$_2$ toward highly efficient and selective electrocatalyst for N$_2$ conversion to NH$_3$ at ambient conditions. *Adv Mater* 2017; **29**: 1606550.
7. Bao D, Zhang Q and Meng F *et al.* Electrochemical reduction of N$_2$ under ambient conditions for artificial N$_2$ fixation and renewable energy storage using N$_2$/NH$_3$ cycle. *Adv Mater* 2017; **29**: 1604799.
8. Qiao B, Wang A and Yang X *et al.* Single-atom catalysis of CO oxidation using Pt$_1$/FeO$_x$. *Nat Chem* 2011; **3**: 634–41.
9. Yang X, Wang A and Qiao B *et al.* Single-atom catalysts: a new frontier in heterogeneous catalysis. *Acc Chem Res* 2013; **46**: 1740–8.
10. Liu P, Zhao Y and Qin R *et al.* Photochemical route for synthesizing atomically dispersed palladium catalysts. *Science* 2016; **352**: 797–800.
11. Wang A, Li J and Zhang T. Heterogeneous single-atom catalysis. *Nat Rev Chem* 2018; **2**: 65–81.
12. Zhang Y. Heterogeneous catalysis: single atoms on a roll. *Nat Rev Chem* 2018; **2**: 0151.
13. Wang Y, Mao J and Meng X *et al.* Catalysis with two-dimensional materials confining single atoms: concept, design, and applications. *Chem Rev* 2019; **119**: 13806–54.
14. Jiao J, Lin R and Liu S *et al.* Copper atom-pair catalyst anchored on alloy nanowires for selective and efficient electrochemical reduction of CO$_2$. *Nat Chem* 2019; **11**: 222–8.
15. Zhang D, Chen Z and Yang W *et al.* MXene (Ti$_3$C$_2$) vacancy confined single-atom catalyst for efficient functionalization of CO$_2$. *J Am Chem Soc* 2019; **141**: 4086–93.

16. Xiong Y, Dong J and Huang Z *et al.* Single-atom Rh/N-doped carbon electrocatalyst for formic acid oxidation. *Nat Nanotechnol* 2020; **15**: 390–7.

17. Zhang L, Ren Y and Liu W *et al.* Single-atom catalysts: a rising star for green synthesis of fine chemicals. *Natl Sci Rev* 2018; **5**: 653–72.

18. Li M, Duanmu K and Wan C *et al. S*ingle-atom tailoring of platinum nanocatalysts for high-performance multifunctional electrocatalysis. *Nat Catal* 2019; **2**: 495–503.

19. Li Z, Ji S and Liu Y *et al.* Well-defined materials for heterogeneous catalysis: from nanoparticles to isolated single-atom sites. *Chem Rev* 2020; **120**: 623–82.

20. Xue Y, Huang B and Yi Y *et al.* Anchoring zero valence single atoms of nickel and iron on graphdiyne for hydrogen evolution. *Nat Commun* 2018; **9**: 1460.

21. Hui L, Xue Y and Yu H *et al.* Highly efficient and selective generation of ammonia and hydrogen on a graphdiyne-based catalyst. *J Am Chem Soc* 2019; **141**: 10677–83.

22. Huang C, Li Y and Wang N *et al.* Progress in research into 2D graphdiyne-based materials. *Chem Rev* 2018; **118**: 7744–803.

23. Li G, Li Y and Liu H *et al.* Architecture of graphdiyne nanoscale films. *Chem Commun* 2010; **46**: 3256–8.

24. Yin H, Dou Y and Chen S *et al.* 2D electrocatalysts for converting earth-abundant simple molecules into value-added commodity chemicals: recent progress and perspectives. *Adv Mater* 2020; **32**: 1904870.

25. Li J, Gao X and Zhu L *et al.* Graphdiyne for crucial gas involved catalytic reactions in energy conversion applications. *Energy Environ Sci* 2020; **13**: 1326–46.

26. Li B, Lai C and Zhang M *et al.* Graphdiyne: a rising star of electrocatalyst support for energy conversion. *Adv Energy Mater* 2020; **10**: 2000177.

27. Gao X, Liu H and Wang D *et al.* Graphdiyne: synthesis, properties, and applications. *Chem Soc Rev* 2019; **48**: 908–36.

28. Liu J, Chen C and Zhao Y. Progress and prospect of graphdiyne-based materials in biomedical applications. *Adv Mater* 2019; **31**: 1804386.

29. Yu H, Xue Y and Hui L *et al.* Efficient hydrogen production on a 3D flexible heterojunction material. *Adv Mater* 2018; **30**: 1707082.

30. Hui L, Xue Y and Huang B *et al.* Overall water splitting by graphdiyne-exfoliated and -sandwiched layered double-hydroxide nanosheet arrays. *Nat Commun* 2018; **9**: 5309.

31. Zhang S, Si H and Fan W *et al.* Graphdiyne omnibearingly bridges the collocation between SnO_2 and perovskite in planar solar cells. *Angew Chem In Ed* 2020; **132**: 2–12.

32. Jia Y, Zhang L and Du A *et al.* Defect graphene as a trifunctional catalyst for electrochemical reactions. *Adv Mater* 2016; **28**: 9532–8.

33. Jia Y, Zhang L and Zhuang L *et al.* Identification of active sites for acidic oxygen reduction on carbon catalysts with and without nitrogen doping. *Nat Catal* 2019; **2**: 688–95.

34. Watt G and Chrisp J. Spectrophotometric method for determination of hydrazine. *Anal Chem* 1952; **24**: 2006–8.

35. Bao D, Zhang Q and Meng FL *et al.* Electrochemical reduction of N_2 under ambient conditions for artificial N_2 fixation and renewable energy storage using N_2/NH_3 cycle. *Adv Mater* 2017; **29**: 1604799.

36. Lv C, Yan C and Chen G *et al.* An amorphous noble-metal-free electrocatalyst that enables nitrogen fixation under ambient conditions. *Angew Chem Int Ed* 2018; **57**: 6073–6.

37. Geng Z, Liu Y and Kong X *et al.* Achieving a record-high yield rate of 120.9 μg_{NH3} mg_{cat}^{-1} h^{-1} for N_2 electrochemical reduction over Ru single-atom catalysts. *Adv Mater* 2018; **30**: 1803498.

38. Tao H, Choi C and Ding L *et al.* Nitrogen fixation by Ru single-atom electrocatalytic reduction. *Chem* 2019; **5**: 204–14.

39. Wang J, Yu L and Hu L *et al.* Ambient ammonia synthesis via palladium-catalyzed electrohydrogenation of dinitrogen at low overpotential. *Nat Commun* 2018; **9**: 1795.

40. Shi MM, Bao D and Li SJ *et al.* Anchoring PdCu amorphous nanocluster on graphene for electrochemical reduction of N_2 to NH_3 under ambient conditions in aqueous solution. *Adv Energy Mater* 2018; **8**: 1800124.

41. Pang F, Wang Z and Zhang K *et al.* Bimodal nanoporous Pd_3Cu_1 alloy with restrained hydrogen evolution for stable and high yield electrochemical nitrogen reduction. *Nano Energy* 2019; **58**: 834–41.

42. Licht S, Cui R and Wang B *et al.* Ammonia synthesis by N_2 and steam electrolysis in molten hydroxide suspensions of nanoscale Fe_2O_3. *Science* 2015; **345**: 637–40.

43. Choi C, Back S and Kim NY *et al.* Suppression of hydrogen evolution reaction in electrochemical N_2 reduction using single-atom catalysts: a computational guideline. *ACS Catal* 2018; **8**: 7517–25.

44. Qiu W, Xie X and Qiu J *et al.* High-performance artificial nitrogen fixation at ambient conditions using a metal-free electrocatalyst. *Nat Commun* 2018; **9**: 3485.

45. Singh AR, Rohr BA and Schwalbe JA *et al.* Electrochemical ammonia synthesis—the selectivity challenge. *ACS Catal* 2017; **7**: 706–9.

46. Li S, Bao D and Shi M *et al.* Amorphizing of Au nanoparticles by CeO_x–RGO hybrid support towards highly efficient electrocatalyst for n_2 reduction under ambient conditions. *Adv Mater* 2017; **29**: 1700001.

47. Wang H, Wang L and Wang Q *et al.* Ambient electrosynthesis of ammonia: electrode porosity and composition engineering. *Angew Chem Int Ed* 2018; **57**: 12360–4.

48. Zhang L, Ji X and Ren X *et al.* Electrochemical ammonia synthesis via nitrogen reduction reaction on a MoS_2 catalyst: theoretical and experimental studies. *Adv Mater* 2018; **30**: 201800191.

49. Liu J, Xiao H and Li J. Constructing high-loading single-atom/cluster catalysts via an electrochemical potential window strategy. *J Am Chem Soc* 2020; **142**: 3375–83.

50. Li J, Li Y and Zhang T. Recent progresses in the research of single-atom catalysts. *Sci China Mater* 2020; **63**: 889–91.